ARTICLES
https://doi.org/10.1038/s41567-020-0854-4
nature physics

Check for updates

Universal scaling of active nematic turbulence

Ricard Alert[1,2,3,4], Jean-François Joanny[5,6,7] and Jaume Casademunt[1,2] ✉

A landmark of turbulence is the emergence of universal scaling laws, such as Kolmogorov's $E(q) \sim q^{-5/3}$ scaling of the kinetic energy spectrum of inertial turbulence with the wavevector q. In recent years, active fluids have been shown to exhibit turbulent-like flows at low Reynolds number. However, the existence of universal scaling properties in these flows has remained unclear. To address this issue, here we propose a minimal defect-free hydrodynamic theory for two-dimensional active nematic fluids at vanishing Reynolds number. By means of large-scale simulations and analytical arguments, we show that the kinetic energy spectrum exhibits a universal scaling $E(q) \sim q^{-1}$ at long wavelengths. We find that the energy injection due to activity has a peak at a characteristic length scale, which is selected by a nonlinear mechanism. In contrast to inertial turbulence, energy is entirely dissipated at the scale where it is injected, thus precluding energy cascades. Nevertheless, the non-local character of the Stokes flow establishes long-range velocity correlations, which lead to the scaling behaviour. We conclude that active nematic fluids define a distinct universality class of turbulence at low Reynolds number.

Turbulent flows exhibit universal statistical properties. Understanding how these properties emerge from the underlying governing equations is a fundamental challenge in non-equilibrium physics. In classic inertial turbulence, energy is injected externally to drive the flows. The nonlinear advective term of the Navier–Stokes equation is responsible for destabilizing the flow and transferring energy from the scales where it is injected to those where it is dissipated. This leads to an energy cascade in the intermediate range of scales, where the flow acquires a scale-invariant structure that manifests as a power-law scaling of the kinetic energy spectrum. Kolmogorov used these arguments in 1941 to derive the universal scaling exponent $-5/3$ for inertial turbulence, independent of the fluid's properties[1,2].

More recently, 'elastic turbulence' was discovered in polymer solutions at low Reynolds numbers, where inertia is negligible[3]. In the past decade, seemingly turbulent flows at low Reynolds numbers have also been discovered in a number of active fluids, mostly of biological origin. Examples include bacterial suspensions[4–8], swarming bacteria[9] and sperm[10], suspensions of microtubules and molecular motors[11–16], epithelial cell monolayers[17–19], and suspensions of artificial self-propelled particles[20,21]. These fluids display spontaneous flows driven by internal active stresses generated by their components at microscopic scales. At high activity, these flows become chaotic, and hence they have been referred to as active turbulence.

Hydrodynamic models for different types of active turbulence have been proposed. Motivated by suspensions of swimming bacteria, some models extend the Toner–Tu equations for polar flocks, thus inheriting their nonlinear alignment and polarity self-advection terms[7,8,22–25]. Active turbulence in these models can be traced back to the same type of advective nonlinearity as in classic inertial turbulence: self-propulsion acts as an effective inertia that transfers energy between scales[26–30]. However, in contrast to inertial turbulence, these models give rise to non-monotonous flow spectra with non-universal scaling exponents, which depend on the values of the model parameters[7,26–28].

A different class of models considers active liquid crystals, with either polar or nematic symmetry. In the polar case, polarity self-advection or other self-propulsion-like terms give rise to oscillatory instabilities that eventually lead to spatio-temporal chaos[31–36]. In the nematic case, however, these terms are not allowed by symmetry. Nevertheless, chaotic flows also appear, driven only by active stresses[37–52]. The balance between active stress and elastic nematic stress defines an intrinsic length that determines the average vortex size[45]. At larger scales, Giomi has proposed the existence of a scaling regime of the flow spectrum[45]. However, such a scaling has not yet been demonstrated.

All together, these previous studies raise the question of whether turbulence in a more classic sense, with scaling behaviour and universal exponents, can exist in active fluids. Here, we show that active nematic fluids can feature turbulent flows with a universal scaling regime at large length scales. Active stresses power an instability that generates spontaneous flow, thereby injecting energy into the flow. We find that the spectrum of energy injection is broad but peaked at an intrinsic wavelength selected by the nonlinear dynamics. We also find that the injected energy is dissipated without being transferred to other scales. Therefore, the scaling regime is not sustained by an energy cascade but by the long-range hydrodynamic interactions of viscous flow.

Minimal hydrodynamic theory of active nematic fluids

We study two-dimensional active nematic fluids at low Reynolds number. Thus, we neglect inertial effects, so that momentum conservation reduces to force balance:

$$0 = -\partial_\alpha P + \partial_\beta(\sigma_{\alpha\beta} + \sigma^{\mathrm{a}}_{\alpha\beta}) \tag{1}$$

The pressure P enforces the incompressibility condition $\partial_\alpha v_\alpha = 0$ of the flow field $\mathbf{v}$, whereas $\sigma_{\alpha\beta}$ and $\sigma^{\mathrm{a}}_{\alpha\beta}$ are the symmetric and antisymmetric parts of the deviatoric stress tensor, respectively. The symmetric part is given by the constitutive equation[53–56]:

$$\sigma_{\alpha\beta} = 2\eta\, v_{\alpha\beta} - \zeta\, q_{\alpha\beta} \tag{2}$$

[1]Departament de Física de la Matèria Condensada, Universitat de Barcelona, Barcelona, Spain. [2]Universitat de Barcelona Institute of Complex Systems (UBICS), Universitat de Barcelona, Barcelona, Spain. [3]Princeton Center for Theoretical Science, Princeton University, Princeton, NJ, USA. [4]Lewis-Sigler Institute for Integrative Genomics, Princeton University, Princeton, NJ, USA. [5]ESPCI Paris, PSL Research University, Paris, France. [6]Laboratoire PhysicoChimie Curie, Institut Curie, PSL Research University, Sorbonne Universités, UPMC, Paris, France. [7]Collège de France, Paris, France. ✉e-mail: jaume.casademunt@ub.edu

where η is the shear viscosity, $v_{\alpha\beta} = 1/2(\partial_\alpha v_\beta + \partial_\beta v_\alpha)$ is the symmetric part of the strain rate tensor, ζ is the active stress coefficient, and $q_{\alpha\beta} = n_\alpha n_\beta - 1/2\delta_{\alpha\beta}$ is the nematic orientation tensor defined by the director field $\hat{\mathbf{n}}$. We assume that the fluid is deep in the nematic phase so that the director has a fixed modulus $|\hat{\mathbf{n}}| = 1$, and components $n_x = \cos\theta$, $n_y = \sin\theta$. For a continuous director field, this constraint precludes the presence or generation of topological defects. Moreover, for the sake of simplicity, we neglect the flow-alignment coupling ($\nu = 0$)[57].

The antisymmetric part of the stress tensor is obtained from angular momentum conservation, and reads[57]:

$$\sigma^{\mathrm{a}}_{\alpha\beta} = \frac{1}{2}(n_\alpha h_\beta - h_\alpha n_\beta) \tag{3}$$

Here, $h_\alpha = -\delta F_n/\delta n_\alpha = K\nabla^2 n_\alpha$ is the orientational field computed from the Frank free energy for nematic elasticity which, in the one-constant approximation, reads[57]:

$$F_n = \frac{K}{2}\int_{\mathcal{A}} (\partial_\alpha n_\beta)(\partial_\alpha n_\beta)\ \mathrm{d}^2\mathbf{r} = \frac{K}{2}\int_{\mathcal{A}} |\boldsymbol{\nabla}\theta|^2\ \mathrm{d}^2\mathbf{r} \tag{4}$$

Finally, the dynamics of the director field reduces to:

$$\partial_t n_\alpha + v_\beta \partial_\beta n_\alpha + \omega_{\alpha\beta} n_\beta = \frac{1}{\gamma} h_\alpha \tag{5}$$

where $\omega_{\alpha\beta} = 1/2(\partial_\alpha v_\beta - \partial_\beta v_\alpha)$ is the vorticity tensor, and γ is the rotational viscosity. The left-hand side is the co-rotational derivative of the director field, whereas the orientational field on the right-hand side specifies the elastic torque acting on the director.

We introduce dimensionless variables by rescaling length by the system size L, time by the active time $\tau_{\mathrm{a}} = \eta/|\zeta|$, pressure by the active stress $|\zeta|$,and orientational field by K/L^2. To eliminate pressure, we take the curl of the force balance equation (1) and obtain a Poisson equation for the vorticity ω, which we can write in terms of the stream function ψ defined by $v_x = \partial_y\psi$, $v_y = -\partial_x\psi$:

$$\nabla^2\omega = -\nabla^4\psi = s(\mathbf{r}, t) \tag{6A}$$

$$s(\mathbf{r}, t) = \frac{1}{2}\frac{R}{A}\nabla^4\theta + S\left[\frac{1}{2}\left[\partial_x^2 - \partial_y^2\right]\sin 2\theta - \partial_{xy}^2\cos 2\theta\right] \tag{6B}$$

This equation describes a Stokes flow stirred by a vorticity source $s(\mathbf{r}, t)$ with two contributions. The first term comes from the antisymmetric stress already present in passive nematic. It accounts for the flow induced by the director relaxation. In contrast, the second term accounts for the active driving. In equations (6A) and (6B), we have defined three dimensionless parameters: the activity number $A \equiv L^2/\ell_c^2$, the viscosity ratio $R \equiv \gamma/\eta$, and the sign of the active stress $S \equiv \zeta/|\zeta| = \pm 1$ for extensile and contractile stresses, respectively. The activity number A compares the system size L to the active length $\ell_c = \sqrt{K/(|\zeta|R)}$ defined by the balance between active and nematic elastic stress.

Finally, in terms of the director angle field θ and the stream function ψ, the director dynamics equation (5) reads:

$$\partial_t\theta + (\partial_y\psi)(\partial_x\theta) - (\partial_x\psi)(\partial_y\theta) + \frac{1}{2}\nabla^2\psi = \frac{1}{A}\nabla^2\theta \tag{7}$$

Equations (6A), (6B) and (7) specify the hydrodynamics of our minimal active nematic fluid. As shown in the Supplementary Note, for a given $S = \pm 1$, the model is left with a single dimensionless parameter $A' = A/(2 + R/2)$. Therefore, R can be fixed without loss of generality. In the numerical simulations, we set $R = 1$. Moreover, for $R = 0$, the model takes a particularly simple form (Supplementary Note).

Stationary flow patterns

The equilibrium solutions of equations (6A), (6B) and (7) are uniformly oriented quiescent states ($\psi = 0$, $\theta = \theta_0$), with spontaneously broken rotational symmetry. These states are unstable to orientational fluctuations, which result in active stress fluctuations. These stresses induce flows that enhance orientational fluctuations, thus giving rise to the so-called spontaneous flow instability[54,58,59]. The growth rate of small perturbations of wavevector $\mathbf{q}$ forming an angle ϕ with the director $\hat{\mathbf{n}}$ reads, in dimensional form:

$$\Omega(\mathbf{q}) = \left[\frac{SA}{2}\cos 2\phi - \left(1 + \frac{R}{4}\right)(qL)^2\right]\tau_{\mathrm{r}}^{-1} \tag{8}$$

where $\tau_{\mathrm{r}} = \gamma L^2/K$. For contractile (extensile) stresses, with $S = -1$ ($S = 1$), the most unstable perturbations are transverse (longitudinal), that is, $\phi = \pi/2(\phi = 0)$, whereas longitudinal (transverse) modulations are stable. Hereafter, we focus on the contractile case ($S = -1$) and we fix $\theta_0 = 0$.

The critical wavelength in the unstable direction, $\lambda_{\mathrm{c}} = 2\pi\ell_{\mathrm{c}}[2+R/2]^{1/2}$, decreases with activity. Therefore, the uniform state becomes unstable when $\lambda_{\mathrm{c}} < L$, that is for $A > A_{\mathrm{c}} = 4\pi^2(2 + R/2)$, with $A_{\mathrm{c}} \approx 100$ for $R = 1$ (Fig. 1a). Right past the instability threshold, only the longest-wavelength mode is unstable, and hence the system evolves into a stripe pattern of wavelength L with a spontaneous shear along the most unstable direction (Fig. 1b). With increasing activity, the amplitude of the pattern increases, and the domain walls, where the flow concentrates, become thinner (Supplementary Note).

At higher activity, the striped pattern undergoes a zig-zag instability that breaks translational invariance along the $\hat{\mathbf{x}}$ direction. The stripes become increasingly undulated and break up into vortices (Fig. 1c, Supplementary Movie 1). For these vortex patterns, reflection symmetry ($\theta \to -\theta$, $y \to -y$, $\psi \to -\psi$) is spontaneously broken. Therefore, a pattern of vortices with the opposite orientation and vorticity is a degenerate solution. At high activity, vortex lattice solutions also exist but they are unstable (Supplementary Note). All these patterns satisfy the condition $\psi = 2\theta/A + c$, with c constant, such that the director angle remains constant along streamlines (Fig. 1c, see Supplementary Note).

Route to turbulence and nonlinear wavelength selection

The vortex patterns remain stable up to values of $A \sim 1{,}500$. For larger activities, we find that the system shows signatures of excitable dynamics[40,60], whereby long transients with slow dynamics are interspersed with rapid rearrangements into a degenerate orientation of the pattern. Further increasing the activity, the pattern becomes increasingly disordered (Fig. 2a) and exhibits persistent dynamics suggestive of spatiotemporal chaos (Supplementary Movie 2). Overall, this sequence of dynamical patterns can be seen as a route from laminar to turbulent flow.

In the disordered chaotic patterns, the spectrum of Frank elastic energy (equation (4), Supplementary equation (29) in Supplementary Note) features a peak at a wavelength independent of system size (Fig. 2b). However, the linear dynamics of the spontaneous-flow instability does not select any intrinsic wavelength but only the direction of the most unstable modes (equation (8) and Fig. 1a) . Therefore, the intrinsic wavelength $\lambda_i \sim \ell_{\mathrm{c}}$ of the patterns (Fig. 2) must be selected by the nonlinear dynamics of the director field (equation (5)). In fact, the nonlinear selection mechanism is based on the dynamics of evolution toward the turbulent state. For example, upon a quench from the uniform state $\theta_0 = 0$ to the highly turbulent regime ($A \gg 5{,}000$), the system

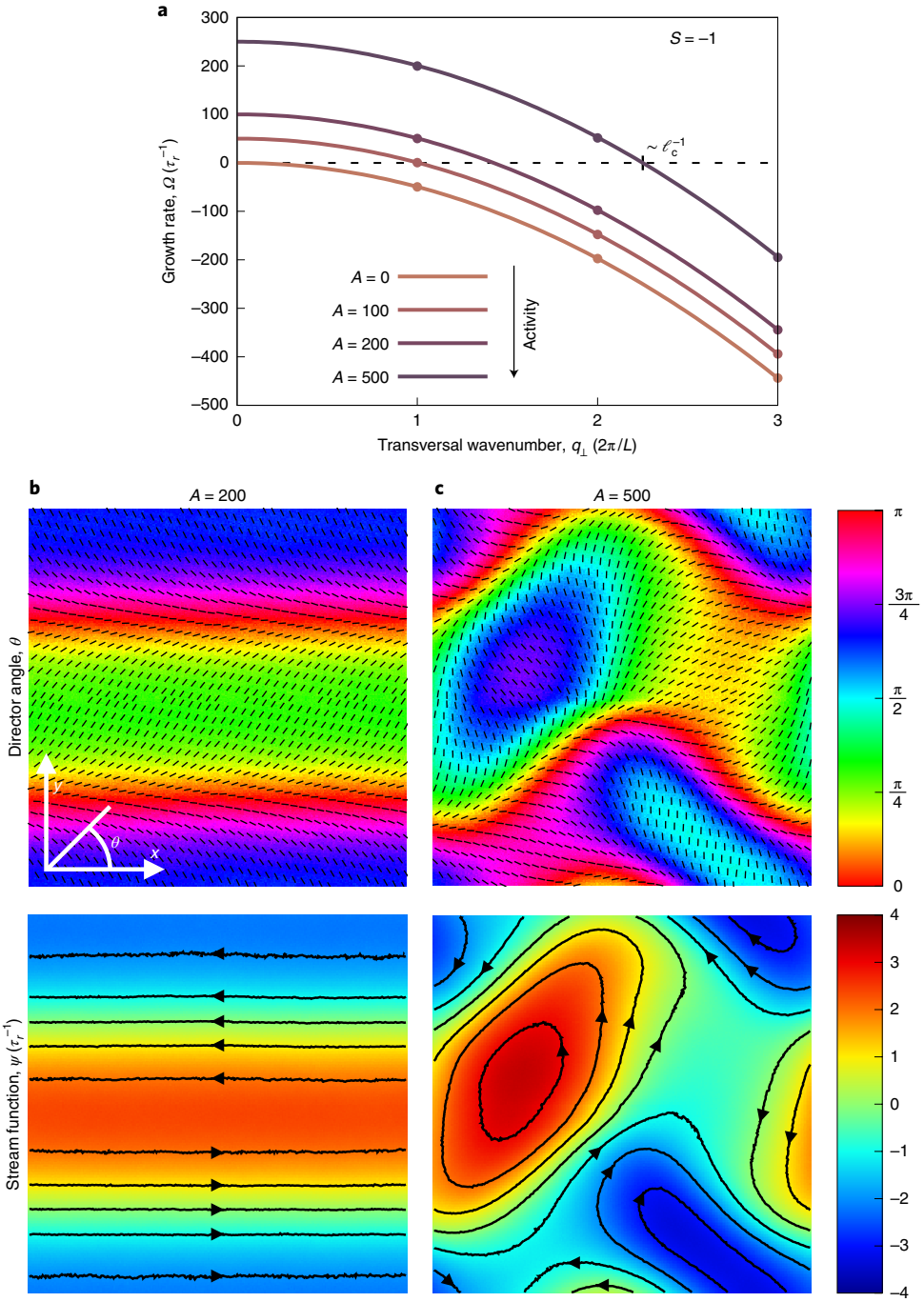

Fig. 1 | Stationary patterns upon the spontaneous flow instability. a, The growth rate, equation (8), of perturbations transverse to the director ($\phi = \pi/2$) for a contractile system ($S = -1$) with $R = 1$. The critical wavelength, which is of the order of the active length ℓ_c, decreases with the activity number A. Points indicate numerical results (Methods), with discrete wavenumbers for a system of size L. **b**, Stripe pattern of the director field (top panel) and the corresponding spontaneous shear flow (bottom panel) for $A = 200$. **c**, Stable pattern of elongated domains of the director field (top panel) and the corresponding spontaneous flow vortices (bottom panel) at higher activity number $A = 500$. Small bars in the top panels indicate the director field. Lines with arrows in the bottom panels indicate streamlines. The director angle is displayed in radians, and the stream function is shown in units of the nematic relaxation time $\tau_r = \gamma L^2/K$.

splits into two quiescent domains of uniform orientation $\theta = \pm\pi/2$ separated by walls of thickness $\sim\ell_c \ll L$ (Supplementary Note). The uniform domains are unstable in the perpendicular direction, and hence they also split. This process continues sequentially until the domain size is comparable to the wall thickness $\sim\ell_c$. Thereby, this transient instability cascade ends up restoring global rotational invariance and selecting a wavelength for the flow pattern. A sequential process similar to this instability cascade was recently observed experimentally[15].

Spectral energy balance

The instability cascade whereby the system becomes turbulent entails a transfer of energy between scales. However, beyond this transient effect, does a stationary transfer of energy exist in active

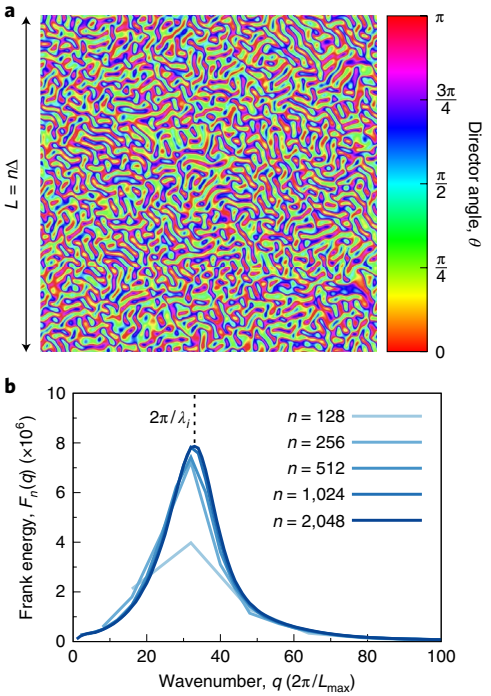

Fig. 2 | Disordered pattern of director domains with a characteristic wavelength. a, Snapshot of the angle field for a system size of 2,048 × 2,048 grid points at activity number $A_{max} = 3.2 \times 10^5$. **b**, The spectrum of the Frank elastic energy, equation (4) (Supplementary equation (29) in Supplementary Note, in units of K/L_{max}) is peaked at an intrinsic wavelength $\lambda_i \sim \ell_c$ independent of system size. Here, ℓ_c is held fixed ($\ell_c = L_{max}/\sqrt{A_{max}} \approx L_{max}/566$), such that the activity number $A = L^2/\ell_c^2$ increases with system size $L = n\Delta$, where Δ is the spacing of the simulation grid points. The wavenumber is rescaled by the largest system size L_{max}, such that the horizontal axis shows the mode number in the largest system ($n = 2{,}048$).

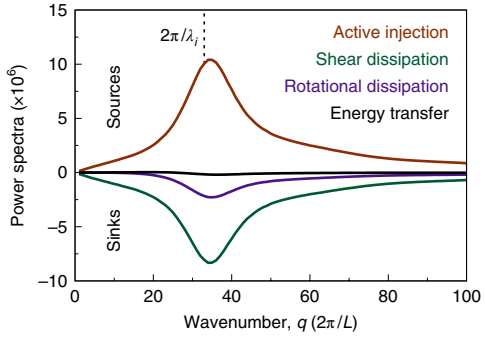

Fig. 3 | Spectra of the four contributions to the energy balance, equation (9) (Supplementary equation (32) in Supplementary Note). These results are for the largest system size with 2,048 × 2,048 grid points at activity number $A = 3.2 \times 10^5$. Supplementary Fig. 2 shows results for smaller systems. The active energy injection is entirely balanced by dissipation at every scale; no energy is transferred between scales. The energy injection rate is maximal at the selected wavelength λ_i. The power spectra are shown in the dimensionless units defined in the text (Supplementary Note).

nematic turbulence? To probe possible energy fluxes across scales, we perform a spectral analysis of energy balance in the stationary turbulent regime. The energy of nematic liquid crystals includes not only the kinetic energy of the flow but also the Frank elastic energy of the director field, F_n. For vanishing Reynolds number, the kinetic contribution vanishes. Thus, the rate of change of the average energy, which vanishes in a statistically stationary state, can be expressed in Fourier space as (Supplementary Note):

$$\dot{F}_n(q) = -D_s(q) - D_r(q) + I(q) + T(q) = 0 \qquad (9)$$

Here, we have separated four contributions: the shear viscous dissipation rate of the flow, $D_s(q)$; the rotational viscous dissipation rate of the director field, $D_r(q)$; the power injected by the active stress, $I(q)$; and the power $T(q)$ transferred from other scales into mode q, which arises from the advection of the director field. The explicit form of these contributions in both real and momentum space are given in the Supplementary Note. In the following, we analyse the spectra of the contributions in equation (9) (Supplementary equation (32) in the Supplementary Note).

In contrast to inertial turbulence, the energy injection is not controlled externally but it is a self-organized process. We find that the active power I has a probability distribution with a positive average, meaning that active stress yields a net injection of energy into the flow (Supplementary Fig. 1). In stationary conditions, the spectral distribution of active energy injection is broad, with a maximum at the selected wavelength λ_i (Fig. 3), where the stored elastic energy is also maximal (Fig. 2b).

Also in contrast to inertial turbulence, the power injection spectrum is balanced by the sum of the dissipation rate spectra locally in Fourier space (Fig. 3). This means that the energy injected at a given scale is entirely dissipated at the same scale. Therefore, there is no energy transfer between scales, and hence no energy cascade. Indeed, using symmetry arguments, we show that the energy transfer term vanishes for all q, $T(\mathbf{q}) = 0$ (Supplementary Note), which we verify numerically (Fig. 3).

Universal scaling

Finally, to study the structure of the turbulent flow, we analyse the spectra of the kinetic energy per mass density, E, and of the enstrophy $\mathcal{E}$:

$$E = \frac{1}{2}\int_{\mathcal{A}} v^2 \, \mathrm{d}^2\mathbf{r}, \qquad \mathcal{E} = \int_{\mathcal{A}} \omega^2 \, \mathrm{d}^2\mathbf{r} \qquad (10)$$

Hereafter, we call E the kinetic energy. The prominent injection of energy at the selected wavelength λ_i gives rise to vortices of that typical size (the small ripples in Fig. 4a). Accordingly, the kinetic energy and the enstrophy spectra (Supplementary equations (35) and (38) in Supplementary Note) exhibit a peak at λ_i (Fig. 4b,c). At wavelengths smaller than this typical vortex size, these spectra respectively scale as $E(q) \sim q^{-4}$ and $\mathcal{E}(q) = 2q^2E(q) \sim q^{-2}$, in agreement with the numerical results and mean-field predictions by Giomi[45]. These scalings characterize the internal structure of the vortices.

At scales larger than λ_i, the system develops large patches of non-coherent but correlated flow with net circulation (large-scale structures in Fig. 4a), each of which encompasses many of the smaller coherent vortices (Supplementary Movie 3). These large-scale structures emerge from the non-local character of Stokes flow. Thereby, local fluctuations of the vorticity source s instantaneously propagate to the whole system through the long-range kernel of equation (6A). As a result, the flow field builds up long-range correlations, and hence the spectrum $E(q)$ should display scale invariance at large length scales.

To extract the scaling exponent from the governing equations, we first analyse the spectrum of the vorticity source $s(\mathbf{r}, t)$, which is ultimately determined by the director field $\theta(\mathbf{r}, t)$ (equation (6B)).

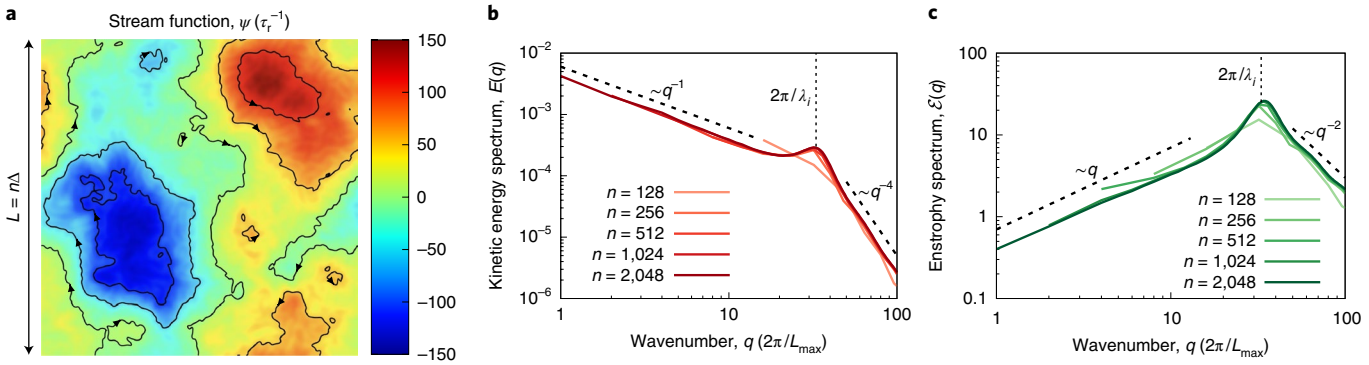

Fig. 4 | Universal scaling of the flow spectra at large scales. a, Snapshot of the stream function field for a system size of 2,048 × 2,048 grid points at activity number $A_{max} = 3.2 \times 10^5$. The stream function is shown in units of the nematic relaxation time $\tau_r = \gamma L^2/K$. The small background ripples correspond to coherent vortices of typical size given by the scale of maximal energy injection λ_i. However, large-scale correlated flow patches also form owing to the non-local character of viscous flow. Lines with arrows indicate a few streamlines that highlight these large-scale circulations. **b**,**c**, The spectra of kinetic energy and enstrophy, equation (10) (Supplementary equations (35) and (38) in Supplementary Note), exhibit a peak at the maximal injection scale λ_i. At smaller scales and, importantly, also at larger scales, the spectra feature distinctive universal scaling regimes. As in Fig. 2b, ℓ_c is held fixed ($\ell_c = L_{max}/\sqrt{A_{max}} \approx L_{max}/566$), such that the activity number $A = L^2/\ell_c^2$ increases with system size $L = n\Delta$, where Δ is the spacing of the simulation grid points. The wavenumber is rescaled by the largest system size L_{max}, such that the horizontal axis shows the mode number in the largest system (n = 2,048). The energy and enstrophy spectra are shown in the dimensionless units defined in the text (Supplementary Note).

The fact that the elastic energy spectrum is peaked and does not exhibit scaling suggests that orientational fluctuations have a finite correlation length. Therefore, we expect $\langle|\tilde{\theta}_{\mathbf{q}}|^2\rangle \sim q^0$ for $q \to 0$. Consequently, from equation (6B), $\langle|\tilde{s}_{\mathbf{q}}|^2\rangle \sim q^4$. Hence, the vorticity source spectrum (Supplementary equation (43) in Supplementary Note) should scale as $\mathcal{S}(q) \sim q\,\langle|\tilde{s}_{\mathbf{q}}|^2\rangle \sim q^5$, which we verified in our simulations (Supplementary Fig. 3). In turn, in Fourier space, equation (6A) reads $-q^2\tilde{\omega}_{\mathbf{q}} = \tilde{s}_{\mathbf{q}}$, and hence $\langle|\tilde{\omega}_{\mathbf{q}}|^2\rangle \sim q^0$ and $\langle|\tilde{\mathbf{v}}_{\mathbf{q}}|^2\rangle = q^{-2}\langle|\tilde{\omega}_{\mathbf{q}}|^2\rangle \sim q^{-2}$. Thus, we find that the kinetic energy and enstrophy spectra scale as $E(q) \sim q\,\langle|\tilde{\mathbf{v}}_{\mathbf{q}}|^2\rangle \sim q^{-1}$ and $\mathcal{E}(q) \sim q\,\langle|\tilde{\omega}_{\mathbf{q}}|^2\rangle \sim q$, which we also verify numerically (Fig. 4b,c).

Discussion and conclusions

In summary, we have introduced a minimal hydrodynamic theory of an active nematic fluid at zero Reynolds number. Based on this theory, we have shown that active fluids can exhibit turbulent flows with universal scaling properties.

To maximize analytical insight and simulation power, we ignored topological defects and the flow-alignment coupling. At scales comparable to the intrinsic active length, the creation and annihilation of topological defects is strongly coupled to the vortex dynamics[43,45,60]. Nevertheless, in agreement with ref. [45], our results show that defects are not essential to understand the large-scale statistics of active turbulence. Moreover, including the flow-alignment coupling does not qualitatively modify the spontaneous flow instability[59] that drives the turbulence. We expect that this coupling can only modify non-universal features such as the structure of vortex patterns and the transition to turbulence, but not the short- or long-range character of correlations. Hence, we believe that our minimal description captures the essential ingredients that determine the universal scaling properties of active nematic turbulence.

In order to understand the route to turbulence, we first studied the emergence of both stationary and turbulent flow patterns. In active nematic fluids, non-uniform director fields generate active stresses that drive spontaneous flows which, in turn, couple to the director field. At moderate values of the dimensionless activity number $A = (L/\ell_c)^2$, this unstable feedback gives rise to stable stationary patterns of orientation domains and flow vortices (Fig. 1) of increasing complexity[48,61]. At higher activity, the system undergoes a transition to turbulence. The turbulent state is characterized by a single characteristic length, $\lambda_i \sim \ell_c$ (Fig. 2). We showed that the wavelength selection mechanism is inherently nonlinear. In contrast, in the active turbulence of generalized flocking models, the vortex size is selected by a linear instability[7,8,22–27,62].

To look for universal features, we studied the large-scale statistical properties of the turbulent flows. In particular, we derived the spectral energy balance in the turbulent regime. We showed numerically that energy injection by the active processes spans all scales, and it is maximal at the selected wavelength λ_i (Fig. 3). At vanishing Reynolds, the injected energy cannot be transferred to other scales by momentum advection as in inertial turbulence[49]. Here we showed that, even in the presence of advection of the director field, our minimal active nematic fluid does not exhibit energy transfer between scales in the stationary turbulent state. The absence of energy transfer is possible because, in active fluids, the spectrum of energy injection is not externally fixed but results from the feedback between the director and the flow fields. As a result, the system self-organizes into a state in which energy injection is exactly balanced by dissipation at each scale. Further research is needed to determine whether flow alignment or topological defects can lead to stationary energy transfer between scales.

Finally, we studied the spectra of kinetic energy and enstrophy of the turbulent flows. Active stresses generate vortices with a characteristic scale. Hence, at the scale λ_i of maximal active injection, the flow spectra feature a peak that reflects the underlying pattern of vortices, in agreement with previous work[45,49]. Based on similar observations, and using mean-field arguments, Giomi predicted that the spectrum of kinetic energy would have a $E(q) \sim q^{-1}$ scaling regime at large scales. However, he could not access sufficiently large scales to verify this prediction in simulations[45]. Here, we leveraged our minimal approach to reach very large-scale simulations that allowed us to conclusively demonstrate this scaling regime (Fig. 4). Moreover, we provide an analytical understanding of the origin of the scaling and of the universal character of its exponent. In the absence of inertia, hydrodynamic interactions are long-range. Thereby, local stresses generate not only coherent vortices of a characteristic size but also large-scale correlated flows. These flows span a range of scales only limited by the system size, as manifested in the scaling behaviour. We derived the scaling laws from the governing equations simply by assuming that the director field has a finite correlation length. Provided that this condition holds, we predict $E(q) \sim q^{-1}$.

In other words, we conclude that, via the long-range hydrodynamic interactions of viscous flow, active processes are able to maintain large-scale modes out of equilibrium and enforce power-law scaling. In this sense[63], chaotic flows in active nematic fluids can be called turbulent. These flows form a distinct class of turbulence at vanishing Reynolds number, in which (1) energy is injected at all scales in a self-organized way, and (2) the flow exhibits universal scale invariance at large scales. In addition, active nematic turbulence can exist without any stationary transfer of energy across scales. This type of active turbulence is thus different from that exhibited by flocking models, which display advective energy cascades[26–30] and parameter-dependent scaling exponents[7,26–28]. Looking forward, we expect that our findings can be tested in large-scale experimental realizations of active nematics.

Online content

Any methods, additional references, Nature Research reporting summaries, source data, extended data, supplementary information, acknowledgements, peer review information; details of author contributions and competing interests; and statements of data and code availability are available at https://doi.org/10.1038/s41567-020-0854-4.

Received: 21 August 2019; Accepted: 19 February 2020;
Published online: 23 March 2020

References

1. Kolmogorov, A. N. The local structure of turbulence in incompressible viscous fluid for very large Reynolds numbers. *Proc. R. Soc. A* **434**, 9–13 (1991).
2. Frisch, U. *Turbulence. The Legacy Of A.N. Kolmogorov* (Cambridge Univ. Press, 1995).
3. Groisman, A. & Steinberg, V. Elastic turbulence in a polymer solution flow. *Nature* **405**, 53–55 (2000).
4. Dombrowski, C., Cisneros, L., Chatkaew, S., Goldstein, R. E. & Kessler, J. O. Self-concentration and large-scale coherence in bacterial dynamics. *Phys. Rev. Lett.* **93**, 098103 (2004).
5. Cisneros, L. H., Cortez, R., Dombrowski, C., Goldstein, R. E. & Kessler, J. O. Fluid dynamics of self-propelled microorganisms, from individuals to concentrated populations. *Exp. Fluids* **43**, 737–753 (2007).
6. Ishikawa, T. et al. Energy transport in a concentrated suspension of bacteria. *Phys. Rev. Lett.* **107**, 028102 (2011).
7. Wensink, H. H. et al. Meso-scale turbulence in living fluids. *Proc. Natl Acad. Sci. USA* **109**, 14308–14313 (2012).
8. Dunkel, J. et al. Fluid dynamics of bacterial turbulence. *Phys. Rev. Lett.* **110**, 228102 (2013).
9. Patteson, A. E., Gopinath, A. & Arratia, P. E. The propagation of active-passive interfaces in bacterial swarms. *Nat. Commun.* **9**, 5373 (2018).
10. Creppy, A., Praud, O., Druart, X., Kohnke, P. L. & Plouraboué, F. Turbulence of swarming sperm. *Phys. Rev. E* **92**, 032722 (2015).
11. Sanchez, T., Chen, D. T. N., DeCamp, S. J., Heymann, M. & Dogic, Z. Spontaneous motion in hierarchically assembled active matter. *Nature* **491**, 431–4 (2012).
12. Henkin, G., DeCamp, S. J., Chen, D. T. N., Sanchez, T. & Dogic, Z. Tunable dynamics of microtubule-based active isotropic gels. *Phil. Trans. R. Soc. A* **372**, 20140142 (2014).
13. Guillamat, P., Ignés-Mullol, J. & Sagués, F. Taming active turbulence with patterned soft interfaces. *Nat. Commun.* **8**, 564 (2017).
14. Lemma, L. M., DeCamp, S. J., You, Z., Giomi, L. & Dogic, Z. Statistical properties of autonomous flows in 2D active nematics. *Soft Matter* **15**, 3264–3272 (2019).
15. Martínez-Prat, B., Ignés-Mullol, J., Casademunt, J. & Sagués, F. Selection mechanism at the onset of active turbulence. *Nat. Phys.* **15**, 362 (2019).
16. Tan, A. J. et al. Topological chaos in active nematics. *Nat. Phys.* **15**, 1033–1039 (2019).
17. Doostmohammadi, A. et al. Cell division: a source of active stress in cellular monolayers. *Soft Matter* **11**, 7328–7336 (2015).
18. Yang, T. D., Kim, H., Yoon, C., Baek, S.-K. & Lee, K. J. Collective pulsatile expansion and swirls in proliferating tumor tissue. *New J. Phys.* **18**, 103032 (2016).
19. Blanch-Mercader, C. et al. Turbulent dynamics of epithelial cell cultures. *Phys. Rev. Lett.* **120**, 208101 (2018).
20. Nishiguchi, D. & Sano, M. Mesoscopic turbulence and local order in Janus particles self-propelling under an ac electric field. *Phys. Rev. E* **92**, 052309 (2015).
21. Karani, H., Pradillo, G. E. & Vlahovska, P. M. Tuning the random walk of active colloids: from individual run-and-tumble to dynamic clustering. *Phys. Rev. Lett.* **123**, 208002 (2019).
22. Dunkel, J., Heidenreich, S., Bär, M. & Goldstein, R. E. Minimal continuum theories of structure formation in dense active fluids. *New J. Phys.* **15**, 045016 (2013).
23. Słomka, J. & Dunkel, J. Generalized Navier-Stokes equations for active suspensions. *Eur. Phys. J. Spec. Top.* **224**, 1349–1358 (2015).
24. Großmann, R., Romanczuk, P., Bär, M. & Schimansky-Geier, L. Vortex arrays and mesoscale turbulence of self-propelled particles. *Phys. Rev. Lett.* **113**, 258104 (2014).
25. Heidenreich, S., Dunkel, J., Klapp, S. H. L. & Bär, M. Hydrodynamic length-scale selection in microswimmer suspensions. *Phys. Rev. E* **94**, 020601 (2016).
26. Bratanov, V., Jenko, F. & Frey, E. New class of turbulence in active fluids. *Proc. Natl Acad. Sci. USA* **112**, 15048–15053 (2015).
27. James, M., Bos, W. J. T. & Wilczek, M. Turbulence and turbulent pattern formation in a minimal model for active fluids. *Phys. Rev. Fluids* **3**, 061101 (2018).
28. Słomka, J. & Dunkel, J. Spontaneous mirror-symmetry breaking induces inverse energy cascade in 3D active fluids. *Proc. Natl Acad. Sci. USA* **114**, 2119–2124 (2017).
29. Słomka, J., Suwara, P. & Dunkel, J. The nature of triad interactions in active turbulence. *J. Fluid Mech.* **841**, 702–731 (2018).
30. Linkmann, M., Boffetta, G., Marchetti, M. C. & Eckhardt, B. Phase transition to large scale coherent structures in two-dimensional active matter turbulence. *Phys. Rev. Lett.* **122**, 214503 (2019).
31. Wolgemuth, C. W. Collective swimming and the dynamics of bacterial turbulence. *Biophys. J.* **95**, 1564–1574 (2008).
32. Giomi, L., Marchetti, M. C. & Liverpool, T. B. Complex spontaneous flows and concentration banding in active polar films. *Phys. Rev. Lett.* **101**, 198101 (2008).
33. Giomi, L. & Marchetti, M. C. Polar patterns in active fluids. *Soft Matter* **8**, 129 (2012).
34. Bonelli, F., Gonnella, G., Tiribocchi, A. & Marenduzzo, D. Spontaneous flow in polar active fluids: the effect of a phenomenological self propulsion-like term. *Eur. Phys. J. E* **39**, 1 (2016).
35. Ramaswamy, R. & Jülicher, F. Activity induces traveling waves, vortices and spatiotemporal chaos in a model actomyosin layer. *Sci. Rep.* **6**, 20838 (2016).
36. Blanch-Mercader, C. & Casademunt, J. Hydrodynamic instabilities, waves and turbulence in spreading epithelia. *Soft Matter* **13**, 6913–6928 (2017).
37. Thampi, S. & Yeomans, J. Active turbulence in active nematics. *Eur. Phys. J. Spec. Top.* **225**, 651–662 (2016).
38. Doostmohammadi, A., Ignés-Mullol, J., Yeomans, J. M. & Sagués, F. Active nematics. *Nat. Commun.* **9**, 3246 (2018).
39. Fielding, S. M., Marenduzzo, D. & Cates, M. E. Nonlinear dynamics and rheology of active fluids: Simulations in two dimensions. *Phys. Rev. E* **83**, 041910 (2011).
40. Giomi, L., Mahadevan, L., Chakraborty, B. & Hagan, M. F. Excitable patterns in active nematics. *Phys. Rev. Lett.* **106**, 218101 (2011).
41. Thampi, S. P., Golestanian, R. & Yeomans, J. M. Velocity correlations in an active nematic. *Phys. Rev. Lett.* **111**, 118101 (2013).
42. Thampi, S. P., Golestanian, R. & Yeomans, J. M. Instabilities and topological defects in active nematics. *Europhys. Lett.* **105**, 18001 (2014).
43. Thampi, S. P., Golestanian, R. & Yeomans, J. M. Vorticity, defects and correlations in active turbulence. *Phil. Trans. R. Soc. A* **372**, 20130366 (2014).
44. Thampi, S. P., Golestanian, R. & Yeomans, J. M. Active nematic materials with substrate friction. *Phys. Rev. E* **90**, 062307 (2014).
45. Giomi, L. Geometry and topology of turbulence in active nematics. *Phys. Rev. X* **5**, 031003 (2015).
46. Thampi, S. P., Doostmohammadi, A., Golestanian, R. & Yeomans, J. M. Intrinsic free energy in active nematics. *Europhys. Lett.* **112**, 28004 (2015).
47. Hemingway, E. J., Mishra, P., Marchetti, M. C. & Fielding, S. M. Correlation lengths in hydrodynamic models of active nematics. *Soft Matter* **12**, 7943–7952 (2016).
48. Doostmohammadi, A., Shendruk, T. N., Thijssen, K. & Yeomans, J. M. Onset of meso-scale turbulence in active nematics. *Nat. Commun.* **8**, 15326 (2017).
49. Urzay, J., Doostmohammadi, A. & Yeomans, J. M. Multi-scale statistics of turbulence motorized by active matter. *J. Fluid Mech.* **822**, 762–773 (2017).
50. Shankar, S. & Marchetti, M. C. Hydrodynamics of active defects: from order to chaos to defect ordering. *Phys. Rev. X* **9**, 041047 (2019).
51. Carenza, L. N., Biferale, L. & Gonnella, G. Multiscale control of active emulsion dynamics. *Phys. Rev. Fluids* **5**, 011302 (2020).
52. Coelho, R. C. V., Araújo, N. A. M. & da Gama, M. M. T. Propagation of active nematic-isotropic interfaces on substrates. Preprint at https://arxiv.org/abs/1911.09410 (2019).
53. Kruse, K., Joanny, J. F., Jülicher, F., Prost, J. & Sekimoto, K. Generic theory of active polar gels: a paradigm for cytoskeletal dynamics. *Eur. Phys. J. E* **16**, 5–16 (2005).

54. Marchetti, M. C. et al. Hydrodynamics of soft active matter. *Rev. Mod. Phys.* **85**, 1143–1189 (2013).
55. Prost, J., Jülicher, F. & Joanny, J.-F. Active gel physics. *Nat. Phys.* **11**, 111–117 (2015).
56. Jülicher, F., Grill, S. W. & Salbreux, G. Hydrodynamic theory of active matter. *Reports Prog. Phys.* **81**, 076601 (2018).
57. de Gennes, P.-G. & Prost, J. *The Physics of Liquid Crystals* 2nd edn (Oxford Univ. Press, 1993).
58. Simha, R. A. & Ramaswamy, S. Hydrodynamic fluctuations and instabilities in ordered suspensions of self-propelled particles. *Phys. Rev. Lett.* **89**, 058101 (2002).
59. Voituriez, R., Joanny, J. F. & Prost, J. Spontaneous flow transition in active polar gels. *Europhys. Lett.* **70**, 404–410 (2005).
60. Giomi, L., Bowick, M. J., Mishra, P., Sknepnek, R. & Marchetti, M. C. Defect dynamics in active nematics. *Phil. Trans. A* **372**, 20130365 (2014).
61. Shendruk, T. N., Doostmohammadi, A., Thijssen, K. & Yeomans, J. M. Dancing disclinations in confined active nematics. *Soft Matter* **13**, 3853–3862 (2017).
62. Słomka, J. & Dunkel, J. Geometry-dependent viscosity reduction in sheared active fluids. *Phys. Rev. Fluids* **2**, 043102 (2017).
63. Falkovich, G. in *Non-equilibrium Statistical Mechanics and Turbulence* Vol. 355 *London Mathematical Society Lecture Note Series* Ch. 1 (eds. Nazarenko, S. & Zaboronsky, O. V.) (Cambridge Univ. Press, 2008).

Publisher's note Springer Nature remains neutral with regard to jurisdictional claims in published maps and institutional affiliations.

© The Author(s), under exclusive licence to Springer Nature Limited 2020

Methods

Numerical scheme. Here we describe the implementation of the numerical integration of our hydrodynamic equations, equations (6A), (6B) and (7). We implement a hybrid numerical scheme that combines a spectral method for the time-independent force balance equations (6A) and (6B) with a generalized version of the Alternating-Direction Implicit (ADI) algorithm[64] for the time evolution of the director dynamics equation (7). To account for fluctuations, we supplement equation (7) with a Gaussian white noise field with $\langle \xi(\mathbf{r},t)\rangle = 0$ and $\langle \xi(\mathbf{r},t)\xi(\mathbf{r}',t')\rangle = 2D\delta(\mathbf{r}-\mathbf{r}')\delta(t-t')$, which we implement by means of a standard stochastic algorithm[65]. We discretize the fields on a grid of $n \times n$ points. We keep a constant grid spacing Δ, and we vary n to change the system size $L = n\Delta$.

At each time step, the scheme computes the numerical Fourier transforms of the director angle field $\theta(\mathbf{r},t)$ and of the nonlinear terms on the right-hand side of equation (6B). We apply the 2/3 rule to prevent aliasing in the Fourier components[64]. From them, we compute the Fourier components of the stream function field $\psi(\mathbf{r},t)$ from the spectral decomposition of equations (6A) and (6B). In dimensionless variables, the Fourier components read:

$$\tilde{\psi}_{\mathbf{q}} = -\frac{R}{2A}\tilde{\theta}_{\mathbf{q}} + \frac{S}{q^4+\epsilon}\left[\frac{q_x^2-q_y^2}{2}\mathcal{F}[\sin 2\theta]_{\mathbf{q}} - q_x q_y \mathcal{F}[\cos 2\theta]_{\mathbf{q}}\right] \qquad (11)$$

where $\mathcal{F}[\cdot]$ indicates the Fourier transform operator, and $\epsilon = 10^{-8}$ is a numerical cut-off to avoid the divergence of the $q = 0$ mode. The Fourier components are then transformed back to real space to update the angle field according to the stochastic version of equation (7). To this end, in addition to adding the noise term, we implemented two modifications of the standard ADI algorithm, which was originally designed to invert only the Laplacian operator. First, we discretize the advective terms in equation (7) by means of centred finite differences. Second, we leverage the Sherman–Morrison formula to impose periodic boundary conditions[64].

Numerical tests. Numerical results were benchmarked against analytical results. In particular, we checked the growth rate, equation (8), as well as the saturation angle θ_s of the transversal stationary patterns, Supplementary equation (8) in Supplementary Note. The integral in Supplementary equation (8) was numerically approximated by summing 10,000 terms of the associated Legendre polynomial[66]:

$$\sqrt{\frac{2A}{4+R}} = 2\pi\sum_{k=0}^{\infty}\left[\frac{(2k-1)!!}{2^k k!}\right]^2 \sin^{2k}\frac{\theta_s}{2} \qquad (12)$$

Numerical details. All numerical integrations have been performed for contractile systems ($S = -1$) with $R \equiv \gamma/\eta = 1$. The amplitude of the angular noise is set to $D = 5\times10^{-4}L^2/\tau_r$. In all cases, the initial condition was a quiescent state with uniform director along the $\hat{\mathbf{x}}$ axis, namely $\theta_0 = 0$. The integration time step is reduced as the number of grid points is increased (Table 1).

Stationary flow patterns. The snapshots of the stationary patterns in Fig. 1b,c were obtained from simulations run for a time $t = 0.4\tau_r$ on a grid of 256×256 points.

Numerical computation of energy and power spectra. All spectra are numerically computed by replacing the ensemble average by an average over 925 snapshots of simulations run for a time $t = 0.1\tau_r$. To allow for temporal decorrelation, the snapshots are taken every $\delta t = 10^{-4}\tau_r$. To allow the system to reach a statistically stationary state, the snapshots are only taken after an initial transient of $t_s = 7.5\times10^{-3}\tau_r$. Using these snapshots, we compute a histogram of the corresponding spectral quantity over wave vector moduli which, for the isotropic correlations of the turbulent state (see Supplementary equation (28) in Supplementary Note), corresponds to the angular average of the spectrum.

Table 1 | Integration time step Δt for simulations with different number of grid points $n \times n$, corresponding to system sizes $L = n\Delta$

n	128	256	512	1,024	2,048
$\Delta t(\tau_r)$	10^{-4}	10^{-5}	5×10^{-6}	10^{-6}	2×10^{-7}

Data availability

All the data presented in this study are available upon request.

Code availability

All the computer code used in this study is available upon request.

References

64. Press, W. H., Teukolsky, S. A., Vetterling, W. T. & Flannery, B. P. *Numerical Recipes in Fortran 77. The Art of Scientific Computing* 2nd edn (Cambridge Univ. Press, 1992).
65. Seeßelberg, M. & Petruccione, F. Numerical integration of stochastic partial differential equations. *Comput. Phys. Commun.* **74**, 303–315 (1993).
66. Chaichian, M., Merches, I. & Tureanu, A. *Mechanics. An Intensive Course* (Springer, 2012).

Acknowledgements

We thank J. Prost for discussions. R.A. thanks A. Frishman for discussions. R.A. acknowledges support from Fundació "La Caixa" and from the Human Frontiers of Science Program (LT000475/2018-C). R.A. thanks J. Prost and acknowledges The Company of Biologists (Development Travelling Fellowship DEVTF-151206) and Fundació Universitària Agustí Pedro i Pons for supporting visits to Institut Curie. J.C. and R.A. acknowledge financial support by MINECO under project FIS2016-78507-C2-2-P and Generalitat de Catalunya under project 2017-SGR-1061. J.C. and J.-F.J. acknowledge support from the Labex Celtisphybio ANR-10-LABX-0038 part of the Idex PSL.

Author contributions

J.C. conceived the research. R.A. and J.C. performed analytical calculations. R.A. performed the simulations. All authors designed the research and interpreted the results. All authors wrote the paper.

Competing interests

The authors declare no competing interests.

Additional information

Supplementary information is available for this paper at https://doi.org/10.1038/s41567-020-0854-4.

Correspondence and requests for materials should be addressed to J.C.

Reprints and permissions information is available at www.nature.com/reprints.